A Modified Linear Integral Resonant Controller for Suppressing Jump-Phenomenon and Hysteresis in Micro-Cantilever Beam Structures

James D.J. MacLean[a,1,*], Sumeet S. Aphale[1,1]

[a] *Centre for Applied Dynamics Research, School of Engineering, University of Aberdeen, Aberdeen, UK*

Abstract

This paper demonstrates the effectiveness of a Modified Linear Integral Resonant Controller (MIRC) based on its original LTI cousin, known just as the 'IRC', for suppressing Jump-Phenomenon and hysteresis found in Micro-Cantilevers. A Method of Multiple Scales frequency response is derived, explored and compared with a Runge-Kutta based numerical integration method in order to understand any shortcomings in approximate analytical methods for the analysis of closed-loop nonlinear systems with the inclusion of a stability analysis. It is found that there exist some mild inconsistencies when comparing closed-loop Method of Multiple Scales to traditional numerical integration. A suitably designed Modified Integral Resonant Controller is implemented in closed-loop. Both analytical and numerical results agree with each other and show significant damping performance. Efficacy of the proposed control scheme is validated via frequency response plots, phase portraits and quiver plots.

1. Introduction

With the advent of micro fabrication in the late 1990's and early 2000's [1], many new Micro-Electromechanical systems (MEMS) were born. MEMS have provided numerous new and innovative ways to measure and interact with systems on the nano and micrometer scale. Cantilever-Nanotubes for sensing tiny mass changes and energy dissipation [2, 3], Comb-Drive Resonators [4, 5] for multi-purpose applications such as; sensing [6], electro-mechanical filtering [7], optical shutters [8], bio sensors [9], micro-grippers [10] and precise voltage measurement [11] and generic Micro-Cantilevers for particle scanning [12], are excellent examples of the progression of modern day technology allowing for the better understanding of nature and the interaction of systems on the nano and micro scales.

*Corresponding author

Email addresses: r02jm18@abdn.ac.uk (James D.J. MacLean), s.aphale@abdn.ac.uk (Sumeet S. Aphale)

Micro-Cantilevers possess multiple nonlinearities such as the cubic nonlinearity and velocity and position squared nonlinearities [12, 2, 3]. The cubic nonlinearity alone introduces a famous resonance effect known as Jump-Phenomenon [13]. Jump-Phenomenon is a sudden change in vibration amplitude in the event of a small excitation frequency shift or change in resonant frequency. The dynamical cause of Jump-Phenomenon is a by-product of multiple different amplitude solutions existing for a single frequency. Some of the amplitude solutions are inherently unstable and thus, the system will force itself to the next nearest stable amplitude solution based on the initial conditions of the micro-cantilever. In sensing based applications [14], the nonlinear dynamics that produce Jump-Phenomenon compromise the consistent and desired operation of the sensing unit itself reducing scanning resolution and in image scanning, produce image artifacts due to these nonlinear behaviours [15]. Under low excitation voltages, these Micro-Cantilevers largely behave akin to linear second order resonant systems and thus are easy to operate and utilise in this specific regime. If one wishes to excite these systems to produce a larger amplitude output for a desired application, this will come at the price of increasing the nonlinearity in the system and hence Jump-Phenomenon will present potential measuring instabilities. In general, many Micro-Cantilevers can be sufficiently described by the Duffing Oscillator because the significant nonlinearities present in their dynamics can be lumped into the nonlinear cubic term that the Duffing Oscillator is described by [16]. This cubic nonlinearity also produces hysteresis based on the input frequency and thus, different amplitude solutions can be reached based on prior initial conditions and is a non-negligible effect. If other significant nonlinearities exist, that cannot be lumped into the cubic nonlinearity term, these nonlinearities are modelled and added to the structure of the Duffing Oscillator [17, 18]. Virtually most MEMS, complicated or simple, possess the same universal cubic nonlinearity and are responsible for the nonlinear resonant effect of Jump-Phenomenon, which arise from Euler-Bernoulli Beam theory derivations [19]. Thusly, the second order resonant differential equation with cubic nonlinearity, derived from Euler-Bernoulli Beam theory coupled with a Galerkin based method, is used in this paper as the default and universal model for the nonlinear vibrations found in MEMS.

A number of effective linear control schemes that impart adequate damping to the system resonance have been reported in literature. These include; Pole Placement Control (PPC) [20], Positive Position Feedback (PPF) [21], Positive Velocity Position Feedback (PVPF) [22] and Integral Resonant Control (IRC) [23]. These controllers can provide a good starting point for providing inspiration into designing equivalent nonlinear controllers. Papers [24, 25, 26] show that an adapted form of PPF can be used to damp, with great success, a primary resonant mode for highly nonlinear Micro-Cantilevers [12]. This, however, comes at the cost of introducing a single sub harmonic resonance and a single super harmonic resonance around the central resonant mode.

Application of the IRC scheme to suppress vibrations in micro-cantilevers has been reported in [25, 27]. In this paper, the same IRC controller proposed by Namavar et al., [23] is modified and adapted for use with nonlinear Micro-

Cantilevers and its effects on nonlinear vibration suppression are expanded upon in significant detail compared to the aforementioned paper[27]. The traditional IRC for linear resonant systems is a robust control design which provides damping under system parameter uncertainties as well as in the event that system damage or alteration occurs. In addition, the design of the IRC for linear resonant systems is always guaranteed to be stable, thus further enhancing its desirable properties as controller. Lastly, the IRC possesses just two tuneable parameters, namely; the 'feed-through' term d and the integral gain k. This greatly simplifies and streamlines the design and the optimisation process for the controller. Omidi and Mahmoodi [26] provide an alternative damping controller to the PPF presented in [12] which does not cause the introduction of sub-harmonic and harmonic resonances about the primary resonant mode by utilising a lossy nonlinear integrator scheme which evolved from the original IRC. In this paper, a new linear modified IRC (MIRC), based on [23], is proposed as solution to damp Jump-Phenomenon as well as the hysteresis effect that comes along with it. The MIRC makes use of the same feed-through and integral gain terms with the addition of a new 'position feedback' term λ. The MIRC presented in this paper also addresses the problem found in [12] in a similar manner to [26], namely not introducing sub and super harmonics around the primary resonance. The advantage of this controller over other nonlinear controllers is the linearity and simplicity of the design. Furthermore, a complete novel dynamical analysis is presented for the proposed MIRC scheme using standard frequency response curves, phase-portraits and vector field quiver plots. These plots are unified in a novel fashion (hitherto not reported in literature to the best of the authors' knowledge) to give an in-depth, intuitive understanding of the open- and closed-loop dynamics.

The remainder of this paper is structured as follows. Section Two details the model of the MEMS cantilever and presents its open-loop frequency response over a range of forcing amplitudes. Section Three presents the design of the proposed damping scheme - Modified IRC (MIRC). Section 4 provides a detailed stability analysis on the closed-loop system using a perturbation method with Jacobian Linearisation. Section Five presents a number of closed-loop results and detailed analysis thereof. Sections Six and Seven conclude the paper.

2. Beam Modelling

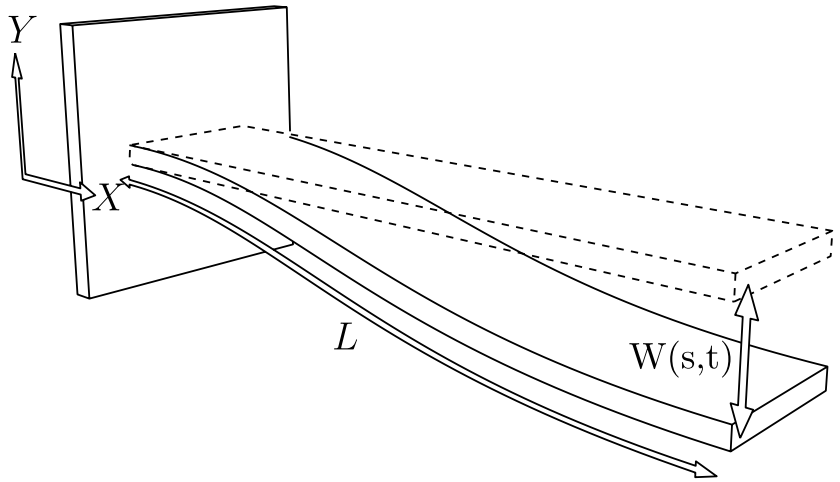

Figure 1: Simplified Micro-Cantilever beam diagram. By applying an electrostatic sinusoidal force to the beam, both nonlinear and linear vibrations will occur in the beam assuming f_0 is large enough. Both these nonlinear and linear vibrations occur around the linear resonant frequency ω_1.

Beam Theory can take two main forms, namely traditional Euler-Bernoulli methods and Hamilton's Principle with the Euler-Lagrange Equation [25, 28, 29]. In paper [25], Hamilton's Principle is used along with the method of separation of variables combined with a Galerkin method [28, 29] to solve for the time differential equation of the cantilever beam. Consider the beam deflection variable, from the neutral X axis, to be $W(s,t)$ (where 's' is the beam length segment from the base of beam at the fixed end, 't' is time and ∂_{var} corrosponds to the relevant partial deriva tive) then the simplified nonlinear PDE from [28, 29] can be shown to be:

$$EI\frac{\partial^4 W}{\partial s^4} + EI\frac{\partial}{\partial s}\left[\frac{\partial W}{\partial s}\frac{\partial}{\partial s}\left[\frac{\partial W}{\partial s}\frac{\partial^2 W}{\partial s^2}\right]\right] + \mu\frac{\partial^2 W}{\partial t^2} + c\frac{\partial W}{\partial t} + \cdots$$
$$\frac{\mu}{2}\frac{\partial}{\partial s}\left[\frac{\partial W}{\partial s}\int_L^s\int_0^s\left[\left(\frac{\partial^2 W}{\partial t\partial s}\right)^2 + \left(\frac{\partial W}{\partial s}\frac{\partial^3 W}{\partial t^2\partial s}\right)\right]dsds\right] = F(s,t) \qquad (1)$$

subject to the following boundary conditions:

$$W(0,t) = \frac{\partial W(0,t)}{\partial s} = 0 \quad \text{at} \quad s = 0, \qquad (2)$$
$$\frac{\partial^2 W(0,t)}{\partial s^2} = \frac{\partial^3 W(0,t)}{\partial s^3} = 0 \quad \text{at} \quad s = L \qquad (3)$$

where E is Young's Modulus ($\mathrm{kgm^{-1}s^{-2}}$), I is the second moment of intertia ($\mathrm{m^4}$), μ is the mass of the beam per unit length ($\mathrm{kgm^{-1}}$), C is a generic internal

damping term (kgs^{-1}), L is the length of the beam (m) and $F(s,t)$ is the forcing function applied to the beam per unit length. By using the separation of variables, $W(s,t)$ can be expressed as the sum of linear combinations of infinitely many modes as follows, namely the combinations of the time based n^{th} amplitude $p_n(t)$ and the n^{th} undamped linear mode shapes $\phi_n(x)$:

$$W(s,t) = \sum_{n=1}^{\infty} \phi_n(s) p_n(t) \tag{4}$$

For this paper, only the first fundamental mode ($n = 1$) is considered. This is due to the fact that micro-cantilevers are primarily affected by their first fundamental mode and harmonics of the fundamental often do not greatly impact the overall response of the system. Since this is the dominant mode for the micro-cantilever, subsequent modes can be ignored. Furthermore, this micro-cantilever, and the corrosponding controller, will be closely around its primary resonant mode which is far from the next harmonic at $n = 2$. The undamped linear mode shapes are derived from equation (1) by ignoring the forcing, nonlinearity and non-conservative damping terms to yield the following linear spatial PDE:

$$EI \frac{\partial^4 W}{\partial s^4} + \mu \frac{\partial^2 W}{\partial t^2} = 0 \tag{5}$$

By substituting in equation (4) into (5), the following spatial ODE can be derived by using the principle of separation of variables:

$$\frac{\partial^4 \phi_n(s)}{\partial s^4} = \beta_n^4 \phi_n(s) \tag{6}$$

where $\beta_n^4 = M\omega_1^2/EI$. Equation (6) has the following general solution:

$$\phi_n(s) = C_{n1} \cosh(\beta_n s) + C_{n2} \sinh(\beta_n s) + C_{n3} \cos(\beta_n s) + C_{n4} \sin(\beta_n s). \tag{7}$$

When applying boundary conditions (2) and (3) to (7), the following formula for the non-trivial solutions is shown to be:

$$1 + \cosh(\beta_n L)\cos(\beta_n L) = 0 \tag{8}$$

Using the aforementioned boundary conditions, the n^{th} mode shape can further be shown to be:

$$\begin{aligned} \phi_n(s) = C_n \Big[&(\cosh(\beta_n s) - \cos(\beta_n s)) + \cdots \\ &\cdots + \frac{\cosh(\beta_n L) + \cos(\beta_n L)}{\sin(\beta_n L) + \sinh(\beta_n L)} \left[\sin(\beta_n s) - \sinh(\beta_n s)\right] \Big]. \end{aligned} \tag{9}$$

It should be noted that the constant C_n is defined as follows using the orthonormality property of mode shapes $\phi_n(s)$:

$$C_n = \int_0^L \phi_n(s)^2 ds = 1 \tag{10}$$

Letting $\beta_n L = \Psi_n$, the formula to produce the resonant frequency of the beam for the mode of interest is:

$$\omega_n = \left(\frac{\Psi_n}{L}\right)^2 \sqrt{\frac{EI}{\mu}} \tag{11}$$

The first numerical solution to equation (8) is $\beta_1 L = \Psi_1 = 1.875...$ which corrosponds to the first fundamental mode's linear frequency. By subtituting equation (4) (for $n = 1$) into equation (1), multiplying the entire equation (1) by $\phi_1(s)$, integrating over the length of the beam L and using the orthonormality properties of linear mode shapes, the resulting non-linear time based ODE is as follows:

$$\begin{aligned} &\ddot{p}_1(t) + 2\zeta\omega_1\dot{p}_1(t) + \omega_1^2 p(t) + \alpha p_1(t)^3 + \cdots \\ &\cdots + \beta\left[p_1(t)^2\ddot{p}_1(t) + p_1(t)\dot{p}_1(t)^2\right] = f(s,t). \end{aligned} \tag{12}$$

The definition for each of the system parameters is as follows:

$$\omega_1^2 = \frac{EI}{\mu}\int_0^L \phi_1(s)\phi_1^{iv}(s)ds \tag{13}$$

$$\alpha = \frac{EI}{\mu}\int_0^L \phi_1(s)\left[\phi_1'(s)\left[\phi_1'(s)\phi_1''(s)\right]'\right]' ds \tag{14}$$

$$\beta = \frac{1}{2}\int_0^L \phi_1(s)\left[\phi_1'(s)\int_L^s\int_0^s \phi_1'(s)^2 ds ds\right]' ds \tag{15}$$

$$2\zeta\omega_1 = \frac{C}{\mu} \tag{16}$$

$$f(s,t) = \frac{1}{\mu}\int_0^L \phi_1(s)F(s,t)ds \tag{17}$$

where $(')$ stands for a single partial spatial derivative and $(^{iv})$ stands for the fourth. The focus of this paper is primarily on the behaviour of the Jump-Phenomenon and hysteresis caused by the cubic nonlinearity term. To this end, equation (17) is assumed to be of sinusoidal forcing. The inertia nonlinearity β is responsible for decreasing the maximum oscillatory amplitude that can obtained while also increasing the fold-over effect where in the resonance curve pushes to one side or the other. To produce open-loop behaviour of the Micro-Cantilever, the Method of Multiple Scales [30] is used on equation (12). The following amplitude resonance polynomial can be derived:

$$\frac{f^2}{4\omega_1^2} = \zeta^2\omega_1^2 a^2 + \left(\frac{1}{8\omega_1}\left(3\alpha - 2\beta\omega_1^2\right)a^3 - \sigma a\right)^2 \tag{18}$$

A full derivation of the above (shown in Section 3), including closed-loop control parameters, is shown in detail later along with a stability analysis which is shown in Section 4. By solving this equation for the perturbation frequency σ instead of the amplitude a, the theoretical frequency response shape, including unstable solutions, can be properly shown. Tab.1 details the parameters used for the following open-loop plot.

Table 1: Open-Loop Parameter Table

	Symbol	Value(s)
Damping Ratio	ζ	0.008
Resonant Frequency	ω_1	10
Curvature Nonlinearity	α	22.5
Inertia Nonlinearity	β	-4.5
Amplitude Values	a	$\{0.0001, \ldots, 0.32\}$

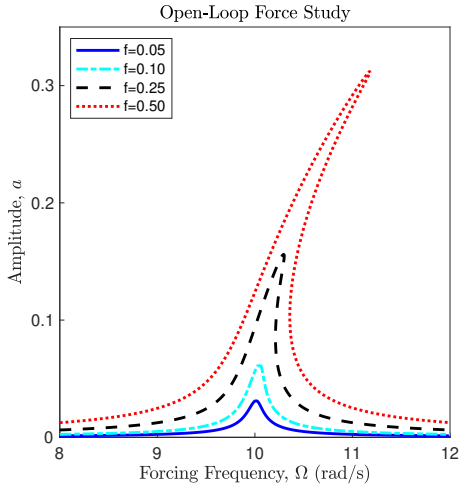

Figure 2: In this open-loop simulation, equation (18) is used to produce the following nonlinear resonance plots. The parameters in Tab.1 are used. Here it is observed that increasing the forcing amplitude causes the nonlinear resonance plot to shift to the right hand side, due to the hardening effect of having a positive α, therefore producing multiple amplitude solutions for the same frequency value namely; two stable and one unstable. The initial conditions determine which stable amplitude the system will gravitate towards and can never settle on the unstable amplitude. As a result of this, this cubic nonlinearity also embodies the effects of hysteresis with the dependence on previous initial conditions.

3. Control Design of the Modified IRC

In order to explain the modification inherent to the MIRC, the original IRC [23] needs to be shown. Consider the following linear resonant second order system that is sinusoidally excited with the closed-loop IRC around it:

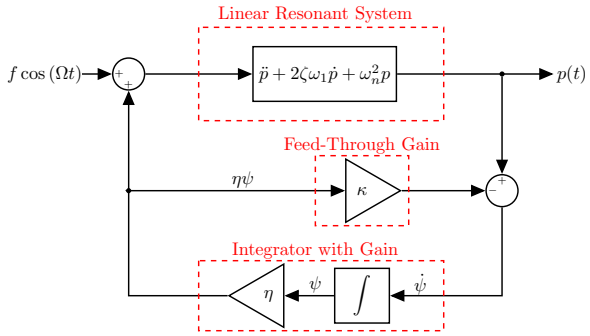

Figure 3: Traditional implementation of the linear Integral Resonant Controller (IRC) on a linear system with lowly-damped resonance. As this is a pure damping controller, the extra input to the system is zero. In the traditional IRC there are two gains, namely; the feed-through gain κ and integrator gain η.

The open-loop parameters used in Fig.3 also partly appear in Tab.1 with the exception of nonlinearity coefficients α and β. The 'Feed-Through Gain' κ is responsible for introducing additional damping to the linear resonance of the system when combined with the linear integrator and gain η. In this paper, to damp the aforementioned Jump-Phenomenon and suppress hysteresis found in nonlinear Micro-Cantilevers, the following Modified-IRC (MIRC) is presented:

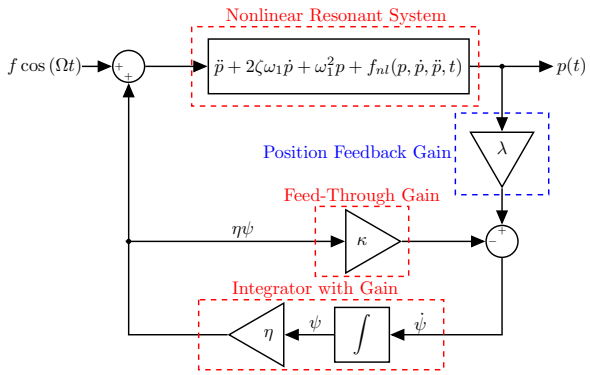

Figure 4: Closed-loop block diagram of the proposed Modified Integral Resonant Control (MIRC) scheme on a system with nonlinear resonant behaviour. The MIRC is still linear and the modification is the introduction of the position feedback gain λ. Here, the extra system term, $f_{nl}(p,\dot{p},\ddot{p},t)$, implies the presence of nonlinearities common to micro-cantilevers and other MEMS.

where the controller variables are; the position feedback gain λ, the feed-through gain κ and the integrator gain η. The addition of the position feedback gain as

seen in Fig.4, highlighted in the feedback path, is an essential new addition to provide extra resonance suppression previously not accomodated by the traditional IRC structure. The closed-loop differential equations for Fig.4 are shown as follows (dropping the subscript of 1 as the first mode is implied);

$$\ddot{p}(t) + 2\zeta\omega_1\dot{p}(t) + \omega_1^2 p(t) + \alpha p(t)^3 + \cdots + \beta\left[p(t)^2\ddot{p}(t) + p(t)\dot{p}(t)^2\right] = f\cos(\Omega t) + \eta\psi(t) \tag{19}$$

$$\dot{\psi}(t) + \kappa\eta\psi(t) = \lambda p(t) \tag{20}$$

In order to analyse the effects of the IRC on the Duffing Oscillator, an approximate analytical perturbation method known as the Method of Multiple Scales [30] as well as traditional numerical integration is used. The primary goal is to conclusively prove that the proposed MIRC adequately damps the nonlinear resonance of the system. By the Method of Multiple Scales, the following definitions are made;

$$\frac{d}{dt} = \frac{\partial}{\partial T_0} + \epsilon\frac{\partial}{\partial T_1} + \cdots \overset{\text{def}}{\approx} D_0 + \epsilon D_1 \tag{21}$$

$$\frac{d^2}{dt^2} = \frac{\partial^2}{\partial T_0^2} + 2\epsilon\frac{\partial^2}{\partial T_0 \partial T_1} + \cdots \overset{\text{def}}{\approx} D_0^2 + 2\epsilon D_0 D_1 \tag{22}$$

$$p(t) \overset{\text{def}}{\approx} p_0(T_0, T_1) + \epsilon p_1(T_0, T_1) + \cdots \tag{23}$$

$$\psi(t) \overset{\text{def}}{\approx} \epsilon\psi_0(T_0, T_1) + \epsilon^2\psi_1(T_0, T_1) + \cdots \tag{24}$$

The Method of Multiple Scales works by splitting linear and damping/nonlinear effects into separate time-scales, namely T_0 (unscaled time) and $T_1 = \epsilon T_0$ (slowed scaled time for some $0 < \epsilon < 1$). The following equations are derived from the expansion above. By substituting in equations (21), (22), (23) and (24) into (19) and (20) the following equations are derived and split in increasing order of ϵ with $O(\epsilon^2)$ being ignored and in addition, the closed-loop system parameters are scaled as follows; $\omega_1 = \hat{\omega}_1$, $\zeta = \epsilon\hat{\zeta}$, $\alpha = \epsilon\hat{\alpha}$, $\beta = \epsilon\hat{\beta}$, $f = \epsilon\hat{f}$, $\kappa = \hat{\kappa}$, $\lambda = \epsilon\hat{\lambda}$ and $\eta = \hat{\eta}$;

$$O(\epsilon^0): D_0^2 p_0 + \hat{\omega}_1^2 p_0 = 0 \tag{25}$$

$$\begin{aligned} O(\epsilon^1): & D_0^2 p_1 + \hat{\omega}_1^2 p_1 = \hat{f}\cos(\Omega T_0) + \hat{\eta}\psi_0 + \cdots \\ & - 2D_0 D_1 p_0 - 2\hat{\zeta}\hat{\omega}_1 D_0 p_0 + \cdots \\ & - \hat{\beta}\left[p_0^2\left(D_0^2 p_0\right) + p_0\left(D_0 p_0\right)^2\right] - \hat{\alpha}p_0^3 \end{aligned} \tag{26}$$

$$O(\epsilon^1): D_0\psi_0 + \hat{\kappa}\hat{\eta}\psi_0 = \hat{\lambda}p_0 \tag{27}$$

It should be noted that the controller variable $\psi(t)$ was upscaled by a factor of ϵ and the controller variables also carefully scaled when compared to a traditional perturbation problem. This was done so that the controller terms do not show

up in the $O(\epsilon^0)$ harmonic oscillator equation as this would produce an incorrect result. Equations (25) and (27) have the following solutions;

$$p_0 = A(T_1)\mathrm{e}^{i\hat{\omega}_1 T_0} + \bar{A}(T_1)\mathrm{e}^{-i\hat{\omega}_1 T_0} \tag{28}$$

$$\psi_0 = \frac{\hat{\lambda}}{\hat{\omega}_1^2 + \hat{\kappa}^2\hat{\eta}^2}\left(\hat{\kappa}\hat{\eta} - i\hat{\omega}_1\right) A(T_1)\mathrm{e}^{i\hat{\omega}_1 T_0} + \overline{\mathrm{CC}} \tag{29}$$

where $\overline{\mathrm{CC}}$ stands for the complex conjugate solution. In order to derive the frequency response for the closed-loop system, solutions (28) and (29) are substituted into (26). The secular terms are the terms that are resonant in the primary resonance ω_n and produce an unbounded solution as per perturbation approximation. By setting the secular terms equal to zero, the frequency response can be derived. Here, the secular terms are derived from the aforementioned subsitutions (note that the sinusoidal forcing term is converted into its complex exponential form). Terms are gathered in terms of powers of $i\omega_n T_0$ and for brevity, it is assumed that $A(T_1) = A$ for space considerations:

$$\begin{aligned} D_0^2 p_1 + \hat{\omega}_1^2 p_1 = \frac{\hat{f}}{2}\mathrm{e}^{i\Omega T_0} + \left[2\hat{\beta}\hat{\omega}_1^2 - \hat{\alpha}\right] A^3 \mathrm{e}^{3i\hat{\omega}_1 T_0} \\ \cdots + \mathcal{S}\mathrm{e}^{i\hat{\omega}_1 T_0} + \overline{\mathrm{CC}} \end{aligned} \tag{30}$$

where $\mathcal{S}$ is the secular resonant term in ω_n and is:

$$\begin{aligned} S = &-\left(3\hat{\alpha} - 2\hat{\beta}\hat{\omega}_1^2\right) A^2 \bar{A} + \cdots \\ &-2i\hat{\omega}_1\left(\hat{\zeta}\hat{\omega}_1 A + D_1 A\right) + \cdots \\ &+\frac{\hat{\eta}\hat{\lambda}}{\hat{\omega}_1^2 + \hat{\kappa}^2\hat{\eta}^2}\left(\hat{\kappa}\hat{\eta} - i\hat{\omega}_1\right) A \end{aligned} \tag{31}$$

To solve for the closed-loop frequency response of the system, the secular and forcing terms are summed and set equal to zero:

$$\frac{\hat{f}}{2}\mathrm{e}^{i\Omega T_0} + \mathcal{S}\mathrm{e}^{i\hat{\omega}_1 T_0} = 0 \tag{32}$$

The following detuning parameter, $\Omega \stackrel{\text{def}}{=} \hat{\omega}_1 + \epsilon\sigma$, is defined in order to simplify equation (32). Remembering that $T_1 = \epsilon T_0$, by substituting in the detuning parameter, equation (32) simplifies to:

$$\frac{\hat{f}}{2}\mathrm{e}^{i\sigma T_1} + \mathcal{S} = 0 \tag{33}$$

To solve for the modulation equations, the amplitude $A(T_1) = A$ is converted to its polar form with:

$$A = \frac{1}{2} a \mathrm{e}^{i\theta} \tag{34}$$

where $a = a(T_1)$ and $\theta = \theta(T_1)$. By substituting in (34) into (33), gathering complex and real part separately and dividing everything by $\mathrm{e}^{i\theta}$, the following modulation equations are derived:

$$\dot{a} = -\left(\hat{\zeta}\hat{\omega}_1 + \frac{\hat{\eta}\hat{\lambda}}{2\left(\hat{\omega}_1^2 + \hat{\kappa}^2\hat{\eta}^2\right)} \right) a + \frac{\hat{f}}{2\hat{\omega}_1} \sin\left(\sigma T_1 - \theta\right) \tag{35}$$

$$\begin{aligned} \dot{\theta} = {} & \frac{1}{8\hat{\omega}_1} \left(3\hat{\alpha} - 2\hat{\beta}\hat{\omega}_1^2 \right) a^2 - \frac{\hat{\kappa}\hat{\eta}^2\hat{\lambda}}{2\hat{\omega}_1\left(\hat{\omega}_1^2 + \hat{\kappa}^2\hat{\eta}^2\right)} + \cdots \\ & \cdots - \frac{\hat{f}}{2\hat{\omega}_1 a} \cos\left(\sigma T_1 - \theta\right) \end{aligned} \tag{36}$$

Another substitution must be made in order to extract the final frequency response as well as the amplitude and phase modulation equations, namely;

$$\Gamma = \sigma T_1 - \theta \quad \text{and} \quad \dot{\Gamma} = \sigma - \dot{\theta} \tag{37}$$

At this point, the scaled circumflex symbol can be dropped from the variables. The final modulation equations can be solved for by substituting in (37) into (36):

$$\dot{a} = -\left(\zeta\omega_1 + \frac{\eta\lambda}{2\left(\omega_1^2 + \kappa^2\eta^2\right)} \right) a + \frac{f}{2\omega_1} \sin\left(\Gamma\right) \tag{38}$$

$$\begin{aligned} a\dot{\Gamma} = {} & -\frac{1}{8\omega_1} \left(3\alpha - 2\beta\omega_1^2 \right) a^3 + \frac{\kappa\eta^2\lambda}{2\omega_1\left(\omega_1^2 + \kappa^2\eta^2\right)} a + \cdots \\ & \cdots + a\sigma + \frac{f}{2\omega_1} \cos\left(\Gamma\right) \end{aligned} \tag{39}$$

Finally, to derive the steady-state frequency response, the modulation equations above are used and the derivative terms $\dot{a}$ and $\dot{\Gamma}$ are set equal to zero and both equations are rearranged for their sine or co-sinusoidal terms. Then both sides, are squared and added:

$$\frac{f^2}{4\omega_1^2} = \left(\zeta\omega_1 + \frac{\eta\lambda}{2\left(\omega_1^2+\kappa^2\eta^2\right)}\right)^2 a^2 + \cdots$$
$$\cdots + \left(\frac{1}{8\omega_1}\left(3\alpha - 2\beta\omega_1^2\right)a^3 - \frac{\kappa\eta^2\lambda}{2\omega_1\left(\omega_1^2+\kappa^2\eta^2\right)}a - \sigma a\right)^2 \tag{40}$$

With the following phase equation:

$$\tan\left(\Gamma\right) = \frac{\left(\zeta\omega_1 + \frac{\eta\lambda}{2\left(\omega_1^2+\kappa^2\eta^2\right)}\right)}{\frac{1}{8\omega_1}\left(3\alpha - 2\beta\omega_1^2\right)a^2 - \frac{\kappa\eta^2\lambda}{2\omega_1\left(\omega_1^2+\kappa^2\eta^2\right)} - \sigma} \tag{41}$$

4. Stability Analysis

In order to produce appropriate stability criteria for the closed-loop system, small perturbations of equations (38) and (39) are considered. The following additional definitions are made for space considerations:

$$\Pi_0 = -\left(\zeta\omega_1 + \frac{\eta\lambda}{2\left(\omega_1^2+\kappa^2\eta^2\right)}\right) \tag{42}$$
$$\Pi_1 = \frac{f}{2\omega_1} \tag{43}$$
$$\Pi_2 = -\frac{1}{8\omega_1}\left(3\alpha - 2\beta\omega_1^2\right) \tag{44}$$
$$\Pi_3 = \frac{\kappa\eta^2\lambda}{2\omega_1\left(\omega_1^2+\kappa^2\eta^2\right)} \tag{45}$$

The following perturbation parameters are used:

$$a = a_0 + a_1 \tag{46}$$
$$\Gamma = \Gamma_0 + \Gamma_1 \tag{47}$$

where a_0 and Γ_0 are constants that satisfy the equilibria of equations (38) and (39) and a_1 and Γ_1 are time dependent perturbation variables from equilibrium. At steady state, equilibria exist thus, equations (38) and (39) become:

$$\Pi_1\sin\left(\Gamma_0\right) = -a_0\Pi_0 \tag{48}$$
$$\Pi_1\cos\left(\Gamma_0\right) = -a_0\left(\Pi_2 a_0^2 + \Pi_3 + \sigma\right). \tag{49}$$

These equations will assist in cancelling out terms found in the following expansion. By substituting equations (46), (47), (48) and (49) into (38) and (39) and only keeping linear terms in a_1 and Γ_1, the following expanded equations are found:

$$\dot{a}_1 = \Pi_0 a_1 + \Pi_2 \cos(\Gamma_0)\,\Gamma_1 \tag{50}$$

$$\dot{\Gamma}_1 = \frac{1}{a_0}\left(\sigma + \Pi_3 + 3\Pi_2 a_0^2\right) a_1 - \frac{\Pi_1}{a_0}\sin(\Gamma_0)\,\Gamma_1. \tag{51}$$

To determine the stability of steady-state solutions, equations (50) and (51) can be represented by a matrix system of equations using the state variable $Z = \begin{bmatrix} a_1 & \Gamma_1 \end{bmatrix}$. Taking the appropriate partial derivatives with respect to the state variables of Z, the linearised state-space system is found to be:

$$\frac{d}{dt}\begin{bmatrix} a_1 \\ \Gamma_1 \end{bmatrix} = \begin{bmatrix} \Pi_0 & -a_0\left(\Pi_2 a_0^2 + \Pi_3 + \sigma\right) \\ \dfrac{1}{a_0}\left(\sigma + \Pi_3 + 3\Pi_2 a_0^2\right) & \Pi_0 \end{bmatrix}\begin{bmatrix} a_1 \\ \Gamma_1 \end{bmatrix} \tag{52}$$

The eigenvalues of (52) can be found by solving $\det(sI - J) = 0$ where I is the 3×3 identity matrix and J is the Jacobian system matrix. Referring to each element of the Jacobian as:

$$J_{11} = \Pi_0 \qquad J_{12} = -a_0\left(\Pi_2 a_0^2 + \Pi_3 + \sigma\right)$$

$$J_{21} = \frac{1}{a_0}\left(\sigma + \Pi_3 + 3\Pi_2 a_0^2\right) \qquad J_{22} = \Pi_0$$

the eigenvalues can be determined by the following stability polynomial:

$$s^2 - (J_{11} + J_{22})\,s + J_{11}J_{22} + J_{12}J_{21} = 0. \tag{53}$$

If any eigenvalue 's' has a negative real part, this indicates an unstable solution and further infers the incorrect choice of controller gains to ensure stability. The criteria for stability are the following:

$$J_{11} + J_{22} < 0 \quad \text{and} \quad J_{11}J_{22} + J_{12}J_{21} > 0 \tag{54}$$

5. Results and Analysis

In this section, equation (40) is used to analyse the theoretical effectiveness of the MIRC's damping capabilities for Micro-Cantilevers. In addition to this, numerical integration using a Runge-Kutta scheme is used as a benchmark to compare the Method of Multiple Scales for closed-loop performance. To understand why the MIRC even produces any damping effects, looking at equation (40) and labelling it is essential:

$$\frac{f^2}{4\omega_1^2} = \overbrace{\left(\zeta\omega_1 + \frac{\eta\lambda}{2\left(\omega_1^2+\kappa^2\eta^2\right)}\right)^2}^{\zeta\omega_1+\text{MIRC}} a^2 + \cdots$$
$$\cdots + \left(\frac{1}{8\omega_1}\left(3\hat{\alpha} - 2\beta\omega_1^2\right)a^3 - \overbrace{\frac{\kappa\eta^2\lambda}{2\omega_1\left(\omega_1^2+\kappa^2\eta^2\right)}}^{\text{MIRC}} a - \sigma a\right)^2$$

For normal linear systems, the traditional IRC effectively serves to increase the damping ratio ζ in the system, thus reducing the maximum resonance amplitude. For highly nonlinear Micro-Cantilevers, this is no different and can be observed by the labelled parts in the frequency response. The MIRC directly adds to the damping ratio ζ term with and also appears in the other half of the frequency response polynomial which theoretically shows why the MIRC can damp even highly nonlinear systems. To demonstrate this, an analytical open- and closed-loop simulation is shown using equation (40). The following micro-cantilever parameters in Tab.2 are used in addition to the parameters used in Tab.1.

Table 2: System and controller parameters used in the simulations.

	Symbol	Value(s)
Forcing Amplitude	f	0.5
Position Feedback Gain	λ	4
Feed-Through Gain	κ	0.1
Integrator Gain	η	10

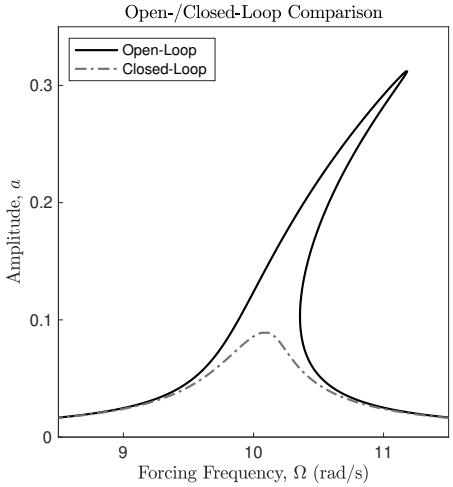

Figure 5: Simulated frequency responses of the open-loop and the MIRC-controlled closed-loop system clearly demonstrate the effectiveness of the proposed control scheme in imparting significant damping to the nonlinear resonance mode of the system.

In this analytical simulation, the suppression of the resonance peak is observed along with the removal of Jump-Phenomenon caused by the cubic nonlinearity term as seen by the closed-loop curve with circle markers (versus the open-loop simulation marked with squares). The effects of the MIRC are immediately apparent due to the significant decrease in maximum amplitude. Additionally, due to the fold-over effect disappearing from the frequency response, this further indicates the removal of the hysteresis effect caused by the cubic nonlinearity. This will later be explored numerically to see if this is true. Furthermore, it should be noticed that for these gains chosen, the DC gain is largely unaffected which is optimal in the sense of preserving non-resonant dynamics and ultimately the DC gain of the system. In this paper, analytical and numerical methods are used to verify the behaviour and effectiveness of the MIRC. Hysteresis is a future state's dependence on a past state and thus, extra care is needed to simulate this numerically. In order to properly simulate the hysteresis in these systems, the following must be in place: for a specific frequency value, wait for the transient to die and produce a limit cycle and then take sample initial conditions from this limit and then repeat this procedure for all future frequency iterations. Repeat this for the same set of frequencies but in reverse. Fig.6 demonstrates a numerically produced frequency response using Runge-Kutta integration with the aforementioned procedures (parameters used are the same as in Tab.2):

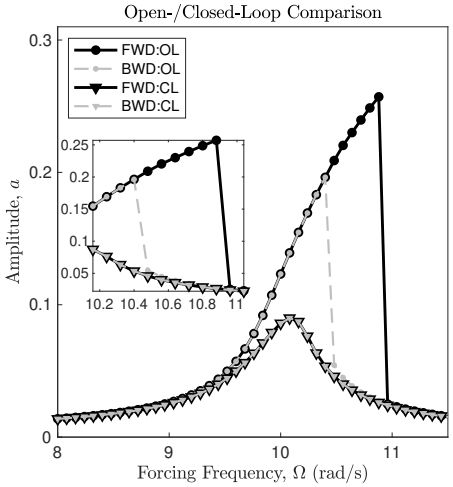

Figure 6: Open- and MIRC-controlled closed-loop frequency responses plotted in the forward and the reverse direction clearly highlights the Jump-Phenomenon present in the system dynamics. 'FWD' stands for a forward frequency sweep. 'BWD' stands for a backward frequency sweep. Here, the circle markers represent open-loop data and the diamond markers represent closed-loop data.

When looking at the open-loop simulation given by the circles, the difference between sweep forward and backward simulations show how different amplitudes can be reached for the exact same frequency depending on previous initial conditions. This is signalled by the grey dotted line and black dashed line showing different paths taken from $\Omega = 10.48\text{rad}\,\text{s}^{-1} \rightarrow 10.96\text{rad}\,\text{s}^{-1}$. They also show the Jump-Phenomenon given by the large changes in amplitude around the linear resonant frequency accompanied by the resonance curve shifting to the right due to the hardening nature of the curvature nonlinearity α being positive and inertia nonlinearity β being negative. The closed-loop plot, given by inverted triangles, shows that there is no dependence on previous initial conditions any more, thus proving the suppression of Jump-Phenomenon and hysteresis. Additionally, there is a decrease in maximum amplitude demonstrating vibration suppression. The λ, η and κ gains are studied in great detail and their effects on the closed-loop system are visualised in the rest of the paper in the same manner as just shown in Fig.5 and Fig.6. The parametric analysis begins with the position feedback gain λ:

Table 3: Simulation parameters for studying the effect of λ on closed-loop behaviour.

	Symbol	Value(s)
Position Feedback Gain	λ_{mms}	$\in \{5, 10\}$
Position Feedback Gain	λ_{num}	$\in \{5, 10\}$
Feed-Through Gain	κ	0.1
Integrator Gain	η	4

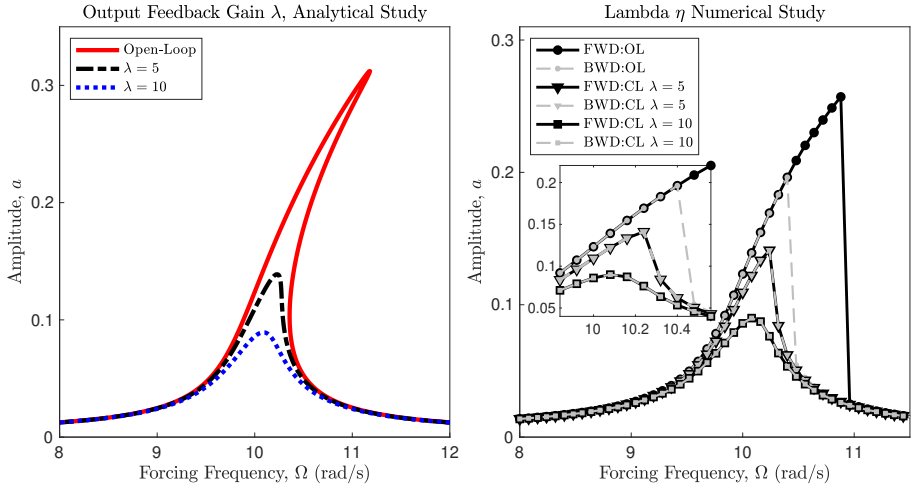

Figure 7: Closed-loop analytical (a) and numerical (b) frequency responses for different values of λ.

In Fig.7(a), the position feedback gain λ is investigated using Tab.3 analytically. By applying the controller value of $\lambda = 5$ there is already a significant decrease in the maximum amplitude, however, this is not enough to suppress Jump-Phenomenon. Increasing this gain further to $\lambda = 10$ shows even greater amplitude suppression along with the removal of Jump-Phenomenon. The removal of Jump-Phenomenon also signals the removal of hysteresis that comes along with it showing the effectiveness of the MIRC's position feedback gain in the suppression of nonlinear effects. In Fig.7(b), a numerical simulation is carried out using the values in Tab.3 where the same values of $\lambda = 5, 10$ are used. For larger λ values, there is strong agreement between both the analytical and numerical results. This comes as a consequence of the Method of Multiple Scales agreeing with numerical results more closely for systems that possess lower amplitudes wherein the hardening effects of the system is minimal. The Method of Multiple Scales exaggerates amplitude values for strongly nonlinear hardening systems. Both the analytical and numerical results agree the same generic trend of the Jump-Phenomenon, hysteresis and amplitude all decreasing with an increasing λ. The next parameter analysed is the integrator gain η.

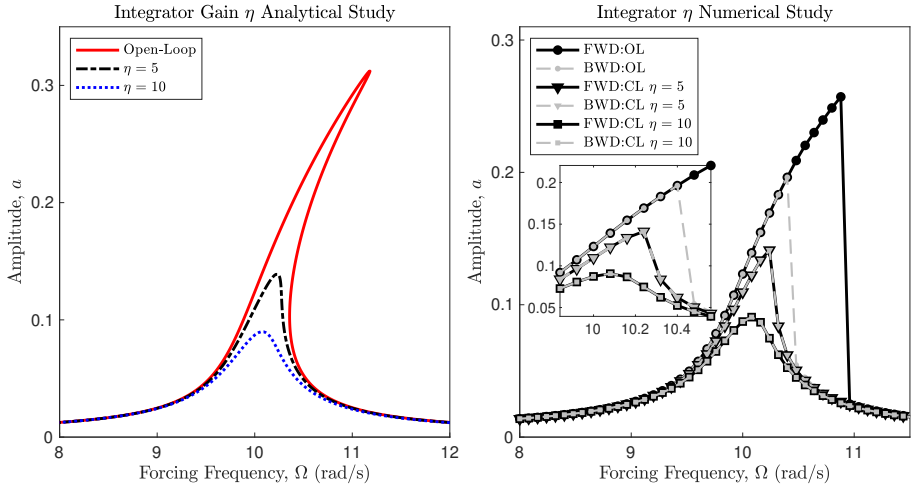

Figure 8: Closed-loop analytical (a) and numerical (b) frequency responses for different η.

Table 4: Simulation parameters for studying the effect of η on closed-loop behaviour.

	Symbol	Value(s)
Integrator Gain	η_{mms}	$\in \{5, 10\}$
Integrator Gain	η_{num}	$\in \{5, 10\}$
Feed-Through Gain	κ	0.1
Position Feedback Gain	λ	4

In Fig.8(a), the integrator gain η is investigated using Tab.4 analytically. By applying the controller value of $\eta = 5$ there is already a significant decrease in the maximum amplitude, however as before, this is not enough to suppress Jump-Phenomenon. Increasing this gain further to $\eta = 10$ shows even greater amplitude suppression along with the removal of Jump-Phenomenon. The removal of Jump-Phenomenon also signals the removal of hysteresis that comes along with it showing the effectiveness of the MIRC's integrator gain in the suppression of nonlinear effects. In Fig.8(b), a numerical simulation is carried out using the values in Tab.4 where the same values of $\eta = 5, 10$ are used. For larger η values, there is about an equal amount of resonance suppression when compared to the analytical results in Fig.8(a). Both gains serve to shift the natural resonance of the system back to where the linear resonance ω_1 is, as seen in both analytical and numerical simulations. Both simulations agree about the same generic trend of the Jump-Phenomenon, hysteresis and amplitude all decreasing with an increasing η or λ. Furthermore, the analytical and numerical simulations of the position feedback and integrator gains shows that the Method of Multiple Scales exaggerates not just open-loop amplitudes, as seen in Fig.5 and Fig.6, but also the suppression of Jump-Phenomenon, hysteresis and the maximum amplitude in the closed-loop case but only when the suppressive effects of the controller are not enforced greatly. Even then, the level of numerical disagreement is strongest in the open-loop case This can be further observed by overlaying the responses of Fig.5 and Fig.6:

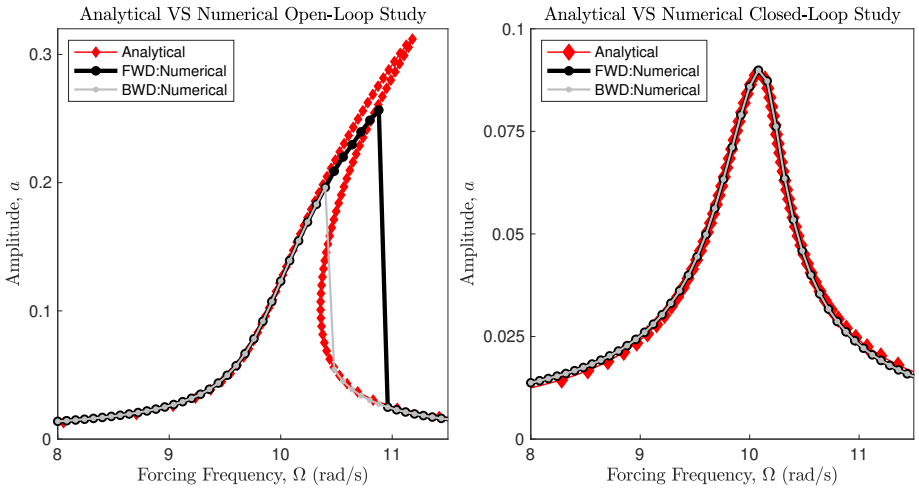

Figure 9: (a) Open-Loop Analytical VS Numerical Integration (b) Closed-Loop Analytical VS Numerical Integration

Fig.9(a) shows that the Method of Multiple Scales is an excellent approximate method for producing realistic open-loop resonance plots that closely agree in behaviour. Even so, the peak amplitudes for the open-loop cases disagree, although this is not unusual, especially in the case of a hardening system like this one. It should also be noted that numerical integration is unable to yield the unstable solutions which can be shown analytically. In the case of the closed-loop case, Fig.9(b) shows that the Method of Multiple Scales and numerical integration agree even more than in the open-loop case and almost perfectly match. Both the Method of Multiple Scales and numerical integration agree on the behaviours that the outpout position feedback and integrator gains each possess. The next parameter analysed is the feed-through gain κ.

Table 5: Simulation parameters for studying the effect of κ on closed-loop behaviour.

	Symbol	Value(s)
Feed-Through Gain	κ_{an}	$\in \{0.1, 5, 10\}$
Feed-Through Gain	κ_{num}	$\in \{0.1, 5, 10\}$
Position Feedback Gain	λ	4
Integrator Gain	η	4

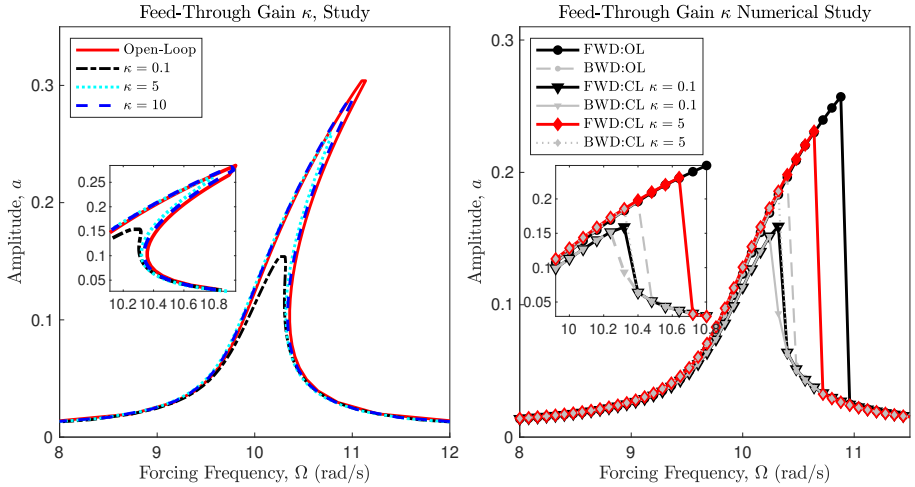

Figure 10: Closed-loop analytical (a) and numerical (b) frequency responses for different values of κ.

In Fig.10(a) the feed-through term κ is investigated using Tab.5. For $\kappa = 0.1$, damping can be observed clearly as with the previous gains. By increasing κ beyond first decimal place values, the system becomes more resonant again which partially undoes any suppressive effects caused by position feedback and integrator gains. For this specific system, there will exist some optimal κ that maximises, for a given η and λ, the damping possible. The numerical analysis in Fig.10(b) also displays the increase in resonance when going beyond $\kappa = 0.1$. As in previous simulations, the exaggeration of the closed-loop amplitudes is apparent and remains an issue with the Method of Multiple Scales in the case where suppression is not at its greatest. Lastly, the removal of hysteresis (and hence the collapse of two stable and one unstable amplitude solutions) due to the MIRC are considered:

Table 6: Parameters used in the limit cycle study presented in Figs. 11.

	Symbol	Value(s)
Position Feedback Gain	λ	10
Feed-Through Gain	κ	0.1
Integrator Gain	η	10

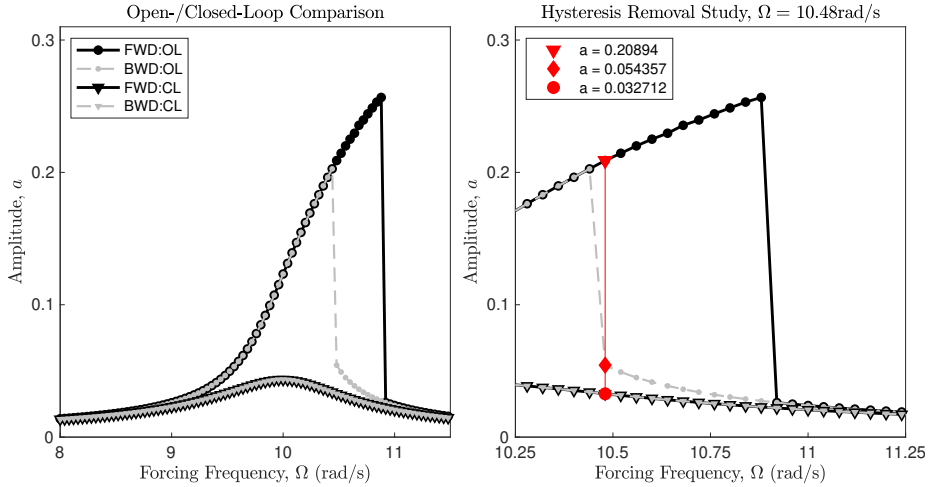

Figure 11: (a) Open- and Closed-Loop Frequency Responses and (b) Zoomed in hysteresis slice around $\Omega = 10.48\text{rad}\,\text{s}^{-1}$

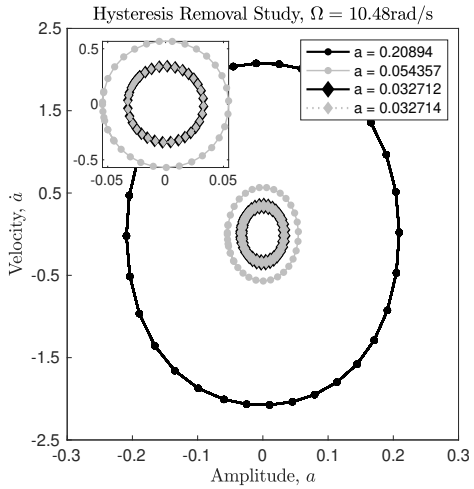

Figure 12: Open- and closed-loop limit cycles plotted for both forward (increasing) and reverse (decreasing) frequency sweeps.

In Fig.11(a), a slice at the frequency of $\Omega = 10.48\text{rad}\,\text{s}^{-1}$ is made in order to show the effects of hysteresis. Fig.11(b) represents a zoomed-in section of the hysteresis region. At this selected frequency for the open-loop case Fig.11(b), it is observed that the sweep forward amplitude ($a_0 \approx 0.21$), marked by a triangle, is much greater than the sweep back amplitude ($a_0 \approx 0.05$) marked by a diamond. This highlights the dependency of the system on previous initial conditions. When applying the MIRC to the system, it can be seen that there exists no hysteresis or Jump-Phenomenon due to the sweep forward and sweep back amplitudes being the same ($a_0 \approx 0.03$, marked with a circle in Fig.11(b))

at this exact chosen frequency (and neighbouring frequencies) highlighting the effectiveness of the controller. The entire hysteresis band has been eliminated by the MIRC. Fig.12 shows the sweep forward and sweep backward phase portraits at this frequency slice for open- and closed-loop scenarios further reinforcing and demonstrating the controller's effect. Notice, that the open-loop sweep forward and sweep back phase portraits (marked by circles) do not coincide. In the case of the closed-loop scenario, the closed-loop sweep forward and sweep back phase portraits (marked by diamonds) do coincide further reinforcing the removal of hysteresis. Previously, it was discussed that the reason for the maximum amplitude decreasing was because of the MIRC effectively adding to the linear damping of the system, however, this does not fully explain the cause for the suppression of multiple solutions, namely the unstable and larger stable solutions, and accompanying hysteresis. Numerical integration by itself is not enough to uncover all the underlying system dynamics as numerical integration cannot reach an unstable amplitude solution. To this end, the analytical equations (38) and (39) are analysed using phase-plane quiver plots and the parameters in Tab.7 in order to demonstrate the existence of the three co-exisiting attractors and classify their local stability. This is again repeated for the closed-loop case.

Table 7: Parameters used in the phase amplitude study.

	Symbol	Value(s)
Forcing Amplitude	f	0.5
Position Feedback Gain	λ	10
Feed-Through Gain	κ	0.1
Integrator Gain	η	4
Phase Values	Γ	$\{-\frac{3}{2}\pi, \ldots, \frac{1}{2}\pi\}$
Amplitude Values	a	$\{0, \ldots, 0.25\}$

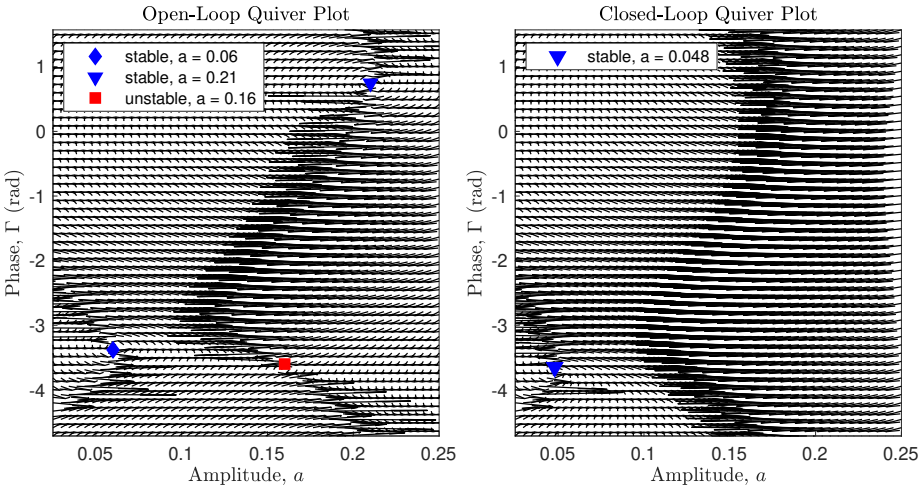

Figure 13: (a) Open-Loop quiver plot showing stable attractors (triangles) and an unstable repellor (square). (b) Closed-loop quiver plot showing a single stable attractor (circle).

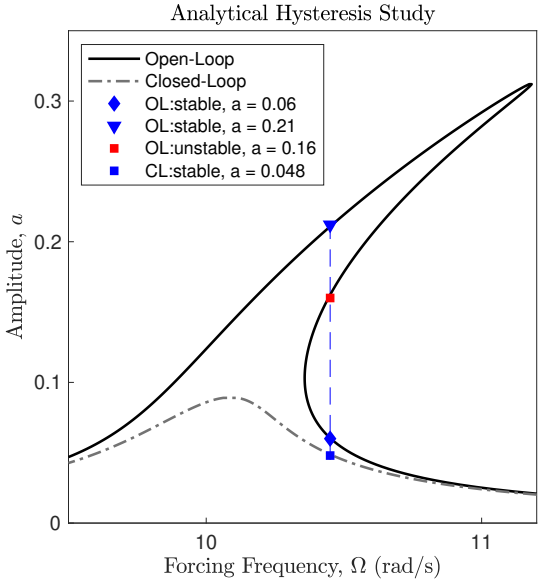

Figure 14: Stable and unstable amplitude-frequency slice for the open- and closed-loop systems.

In Fig.13(a) there exist two stable attractors and one unstable repellor. At the bottom left and top right, exist the two stable amplitude solutions of $a_0 \approx 0.06$ and $a_0 \approx 0.21$ respectively, shown by triangles, which are directly related to the values Fig.14. The bottom right, given by a square, demonstrates unstable saddle-node at amplitude $a_0 \approx 0.16$. This plot highlights the reason for the existence of hysteresis as a whole. When the system moves from one frequency

to another it has the chance, depending on initial conditions, to land near any one of the attractors or near the repeller, or even bounce between either of the stable attractors due to forcing frequency shifts. When applying the MIRC to the system, Fig.13(b) shows that only one stable attractor remains (at $a_0 \approx 0.048$). This is the complete reason for the removal of Jump-Phenomenon and the hysteresis that comes with it.

6. Conclusion

In conclusion, a Modified Integral Resonant Controller is implemented for use with micro-cantilevers which allows for the suppression of amplitude, Jump-Phenomenon and the accompanying hysteresis. A Method of Multiple Scales analysis is combined with Runge-Kutta based numerical simulations in order to verify the behaviours of the open-loop system and each of the closed-loop gains that the MIRC possesses. The output feedback and integrator gains, λ and η respectively, possess the ability to suppress the nonlinear resonance inherent in the system. Appropriate choices of these gains can completely remove jump-phenomenon and hysteresis. The feed-forward gain κ, also provides an important factor when it comes to the damping of the closed-loop system. It is observed that small values of κ produce better damping than larger values above 0.1. When moving beyond this value, the system becomes more resonant again thus partially undoing any damping the previous two gains had achieved. This is confirmed both analytically and via numerical integration. When applying the MIRC, the nonlinear resonance plot begins to shift back to the left where the original linear resonance is located. This shift can be tuned, at will if needed, to move the system back to being a pseudo linear second order resonant system once more.

An important finding is the exaggeration of open-loop, and weakly damped closed-loop, amplitudes that the Method of Multiple Scales provides when comparing with numerical results. In the analytical plots produced, the cases of; open-loop, smaller λ and η all produced a greater maximum amplitude when compared with their numerically integrated counterparts. This is a downside to the Method of Multiple Scales when it comes to analysing highly nonlinear hardening system where the maximum amplitude achieved is actually lower. Regardless, when it came to sufficiently damped closed-loop plots, the Method of Multiple Scales and numerical integration both agreed almost exactly showing the strength of the Method of Multiple Scales.

A complete analytical and numerical analysis is provided in order to uncover why the MIRC can remove jump-phenomenon and hysteresis. It is found that the MIRC, with appropriately chosen gains, removes two key pieces of dynamics inherent to the system, namely; an unstable repellor and a larger stable attractor. It is these dynamics that produce the hysteresis and jump-phenomenon by creating a prior dependence on initial conditions. By removing these dynamics via the MIRC, the system is left with a single stable attractor to which the system will always evolve to no matter the initial conditions. These findings were demonstrated in a novel way (hitherto not reported in literature to

the best of the authors' knowledge) by combining; nonlinear resonance plots, phase portraits and quiver plots together to create a full dynamical understanding for both open- and closed-loop behaviours. Both numerical and analytical methodologies were needed to uncover all the details of the MIRC's effects on the micro-cantilever dynamics.

7. Further Work

As a result of the findings in this paper, there is the potential for new work across different disciplines, namely; an experimental verification of the MIRC on a cantilever beam undergoing large deflections, investigate the effect of disturbances on the performance of the MIRC and to investigate the effects of other damping controllers on the micro-cantilever and determine if they provide better damping performance, without comprimising control input or introducing unwanted dynamics.

References

[1] S. Fransilla, Introduction to Microfabrication, 2nd Edition, Wiley, (2010).

[2] H. Cho, M.-F. Yu, A. F. Vakakis, L. A. Bergman, D. M. McFarland, Tunable, Broadband Nonlinear Nanomechanical Resonator, Nano Letters (2010).

[3] H. Cho, B. Jeong, M.-F. Yu, A. F. Vakakis, D. M. McFarland, L. A. Bergman, Nonlinear hardening and softening resonances in micromechanical cantilever-nanotube systems originated from nanoscale geometric nonlinearities, International Journal of Solids and Structures (2012).

[4] R. Legtenberg, A. W. Groeneveld, M. Elwenspoek, Comb-drive actuators for large displacements, Journal of Micromechanics and Microengineering (1996).

[5] A. M. Elshurafa, K. Khirallah, H. H. Tawfik, A. Emira, A. K. S. A. Aziz, S. M. Sedky, Nonlinear Dynamics of Spring Softening and Hardening in Folded-MEMS Comb Drive Resonators, Journal of Microelectromechanical Systems (2011).

[6] M. Moradi, S. Sivoththaman, Design and Modeling of a Chevron MEMS Strain Sensor With High Linearity and Sensitivity, IEEE Sensors Journal (2015).

[7] I. C. Reines, C. L. Goldsmith, C. D. Nordquist, C. W. Dyck, G. M. Kraus, T. A. Plut, P. S. Finnegan, F. Austin, C. T. Sullivan, A low loss RF MEMS Ku-band integrated switched filter bank, IEEE Microwave and Wireless Components Letters (2005).

[8] J. Zawadzka, L. Li, D. Uttamchandani, Characterisation of a nanostepper driven optical shutter for application in free-space microoptics, IEE Proceedings - Science, Measurement and Technology (2004).

[9] R. Chowdhury, S. Adhikari, J. Mitchell, Vibrating carbon nanotube based bio-sensors, Physica E: Low-dimensional Systems and Nanostructures (2009).

[10] C. . Kim, A. P. Pisano, R. S. Muller, Silicon-processed overhanging microgripper, Journal of Microelectromechanical Systems (1992).

[11] P. S. Riehl, K. L. Scott, R. S. Muller, R. T. Howe, J. A. Yasaitis, Electrostatic charge and field sensors based on micromechanical resonators, Journal of Microelectromechanical Systems (2003).

[12] J. Warminski, M. Cartmell, M. Bochenski, I. Ivanov, Analytical and experimental investigations of an autoparametric beam structure, Journal of Sound and Vibration 315 (2008) pp.486–508. EUROMECH colloquium 483, Geometrically non-linear vibrations of structures.

[13] M. J. Brennan, A. C. I. Kovacic, T. P. Waters, On the jump-up and jump-down frequencies of the Duffing oscillator, Journal of Sound and Vibration (2008).

[14] S. M. Hosseini, A. Shooshtari, Nonlinear-forced vibrations of piezoelectrically actuated viscoelastic cantilevers, Nonlinear Dynamics (2014).

[15] Y. K. Yong, A. G. Fowler, A. Mohammadi, S. O. R. Moheimani, Control of a MEMS Nanopositioner for Atomic Force Microscopy, IFAC Proceedings Volumes 46 (2013) pp.375–382. 6th IFAC Symposium on Mechatronic Systems.

[16] D. K. Agrawal, J. Woodhouse, A. A. Seshia, Modeling nonlinearities in MEMS oscillators, IEEE Transactions on Ultrasonics, Ferroelectrics, and Frequency Control 60 (2013) pp.1646–1659.

[17] H.-T. Yau, C.-C. Wang, C.-T. Hsieh, C.-C. Cho, Nonlinear analysis and control of the uncertain micro-electro-mechanical system by using a fuzzy sliding mode control design, Computers & Mathematics with Applications 61 (2011) pp.1912–1916. Advances in Nonlinear Dynamics.

[18] S. Sabarathinam, K. Thamilmaran, Implementation of analog circuit and study of chaotic dynamics in a generalized duffing-type mems resonator, Nonlinear Dynamics 87 (2017) pp.2345–2356.

[19] J. Warminski, M. Bochenski, W. Jarzyna, P. Filipek, M. Augustyniak, Active suppression of nonlinear composite beam vibrations by selected control algorithms, Communications in Nonlinear Science and Numerical Simulation 16 (2011) pp.2237 – 2248. Biological and Mechanical Systems in Modern Control Theory.

[20] P. T. Kabamba, S. M. Meerkov, E. . Poh, Pole placement capabilities of vibrational control, IEEE Transactions on Automatic Control (1998).

[21] R. J. Moon, A. San-Millan, M. Aleyaasin, V. Feliu, S. S. Aphale, Selection of Positive Position Feedback Controllers for Damping and Precision Positioning Applications. (Best Paper Award Finalist), Springer, 2017, pp. pp.289–301.

[22] D. Russell, A. J. Fleming, S. S. Aphale, Simultaneous Optimization of Damping and Tracking Controller Parameters Via Selective Pole Placement for Enhanced Positioning Bandwidth of Nanopositioners, Journal of Dynamic Systems, Measurement, and Control (2015).

[23] M. Namavar, A. J. Fleming, M. Aleyaasin, K. Nakkeeran, S. S. Aphale, An Analytical Approach to Integral Resonant Control of Second-Order Systems, IEEE/ASME Transactions on Mechatronics (2014).

[24] W. A. El-Ganaini, Saeed, N. A., M. Eissa, Positive position feedback (PPF) controller for suppression of nonlinear system vibration, Nonlinear Dynamis (2013).

[25] E. Omidi, S. N. Mahmoodi, Nonlinear vibration suppression of flexible structures using nonlinear modified positive position feedback approach, Nonlinear Dynamics (2015).

[26] E. Omidi, S. N. Mahmoodi, Nonlinear integral resonant controller for vibration reduction in nonlinear systems, Acta Mechanica Sinica (2016).

[27] E. Omidi, S. N. Mahmoodi, Sensitivity analysis of the Nonlinear Integral Positive Position Feedback and Integral Resonant controllers on vibration suppression of nonlinear oscillatory systems, Communications in Nonlinear Science and Numerical Simulation 22 (2015) pp.149–166.

[28] S. N. Mahmoodi, N. Jalili, M. F. Daqaq, Modeling, Nonlinear Dynamics, and Identification of a Piezoelectrically Actuated Microcantilever Sensor, IEEE/ASME Transactions on Mechatronics 13 (2008) pp.58,65.

[29] S. N. Mahmoodi, N. Jalili, M. F. Daqaq, Modeling, Nonlinear Dynamics, and Identification of a Piezoelectrically Actuated Microcantilever Sensor, IEEE/ASME Transactions on Mechatronics (2008).

[30] A. H. Nayfeh, The Method of Multiple Scales, Wiley-Blackwell, (2007), pp. pp.228–307.